JACS
JOURNAL OF THE AMERICAN CHEMICAL SOCIETY

Ab Initio Prediction of Adsorption Isotherms for Small Molecules in Metal–Organic Frameworks: The Effect of Lateral Interactions for Methane/CPO-27-Mg

Kaido Sillar[†] and Joachim Sauer*

Institut für Chemie, Humboldt-Universität zu Berlin, 10099 Berlin, Germany

Supporting Information

ABSTRACT: A hybrid method that combines density functional theory for periodic structures with wave function-based electron correlation methods for finite-size models of adsorption sites is employed to calculate energies for adsorption of CH_4 onto different sites in the metal–organic framework (MOF) CPO-27-Mg (Mg-MOF-74) with chemical accuracy. The adsorption energies for the Mg^{2+}, linker, second layer sites are −27.8, −18.3, and −15.1 kJ/mol. Adsorbate–adsorbate interactions increase the average CH_4 adsorption energy by about 10% (2.4 kJ/mol). The free rotor-harmonic oscillator-ideal gas model is applied to calculate free energies/equilibrium constants for adsorption on the individual sites. This information is used in a multisite Langmuir model, augmented with a Bragg–Williams model for lateral interactions, to calculate adsorption isotherms. This ab initio approach yields the contributions of the individual sites to the final isotherms and also of the lateral interactions that contribute about 15% to the maximum excess adsorption capacity. Isotherms are calculated for both absolute amounts, for calculation of isosteric heats of adsorption as function of coverage, and excess amounts, for comparison with measured isotherms. Agreement with observed excess isotherms is reached if the experimentally determined limited accessibility of adsorption sites (78%) is taken into account.

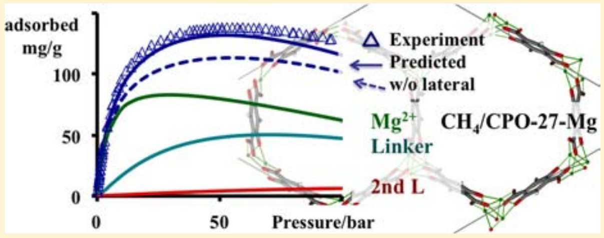

1. INTRODUCTION

To meet environmental standards and to reduce the dependence on oil-based petroleum, natural gas (which mainly consists of methane) is considered as alternative fuel for transport applications. The available means of on-board storage of methane, liquefying and compressing, have the major drawback of consuming themselves a considerable amount of energy. It seems more efficient to adsorb methane into porous solids, which, because of the gas–solid interactions, store more gas molecules than an empty container would under the same conditions. This excess adsorption is proportional to the specific surface area of the adsorbents and depends on the strength of the interaction between the gas molecules and the surface.[1,2] Among the porous materials, the crystalline metal–organic frameworks (MOFs) have exceptionally high surface areas (even exceeding 5000 or 6000 m^2/g),[3−6] and high methane storage capacities have been reported[7−17] in particular for MOFs with a high density of accessible strong adsorption sites at the pore surfaces, typically under-coordinated metal cations.[9−11] By now the highest methane storage capacity[11] (195 cm^3(STP)/cm^3) at 298 K has been reported for CPO-27-Ni, the Ni^{2+}-containing member of the CPO-27-M series of isostructural compounds. On the basis of composition, these framework structures are also named M_2(dhtp), where M is a divalent metal and dhtp refers to the fully deprotonated form of 2,5-dihydroxyterephthalic acid (H_4dhtp).[18−21] The zinc analogue is referred to as MOF-74.[18] As a lighter material with the highest gravimetric adsorption capacity in the CPO-27 family, CPO-27-Mg is of particular interest for transport applications.[11]

Because the maximum adsorption capacities of most of the known MOFs are still below the target set by DOE, 180 cm^3(STP)/cm^3, corresponding to the energy density of compressed methane at 200 bar, the search for improved storage materials goes on and even gains momentum. Not only has the simulation of adsorption isotherms[22] become a valuable tool in the design of new structures with improved adsorption properties, it can also help to find the reasons why in a known material not all adsorption sites of the ideal structure are accessible.[11,21,23,24] For example, in CPO-27 with Ni^{2+} and Mg^{2+} only 92 and 78% of strong adsorption sites, respectively, are accessible.[11] The reason for this is not clear but may be due to incomplete activation (partial removal of water or other solvent molecules from the metal cation sites) or to the presence of defects in the crystal structure that restrict the access to some of the pores. Thus, the evaluation of adsorption properties of the fully activated, i.e., ideal material by computational means is very desirable. This will be done in the present study for adsorption of CH_4 in CPO-27-Mg, which is of interest also from a fundamental surface science point of view. The Mg^{2+} sites in CPO-27 share the five-fold oxygen coordination with the terrace sites on the MgO(001) surface,[25]

Received: July 19, 2012
Published: September 12, 2012

dx.doi.org/10.1021/ja307076t | J. Am. Chem. Soc. 2012, 134, 18354−18365

with a higher site density on the surface and a much smaller surface area in the latter case.

For various MOFs, methane adsorption isotherms have been calculated using grand-canonical Monte Carlo (GCMC) simulations.[2,22] The latter requires millions of energy calculations which are only possible if parametrized potentials (force fields) are used. Most of them are parametrized on experimental data and, hence, may be affected by imperfections of the samples used. This problem can be avoided when fitting to the results of quantum chemical calculations, see ref 26 for a recent promising example. Although fully flexible force fields for selected MOFs have been developed,[27−30] GCMC simulations are carried out for frameworks that are kept frozen, either at their experimentally determined structures[31,32] or at structures determined computationally.

We will use a method for ab initio predictions of adsorption isotherms that is based on a multi-Langmuir adsorption model, molecular statistics, and accurate quantum chemical calculations of binding energies for the interaction of single molecules on the individual binding site[33] and, hence, avoids the drawbacks connected with "effective" empirical potentials and the neglect of quantum effects. The multi-Langmuir model combines individual adsorption isotherms for different types of adsorption sites into an overall isotherm. For H_2 adsorption this model worked well[33] because H_2−H_2 interactions are very weak, and all adsorption sites can be considered as independent. For CH_4 adsorption, adsorbate−adsorbate interactions cannot be ignored. We use the Bragg−Williams model[34,35] to include them and find that lateral interactions not only change the energy term but also the entropy term with a significant effect on the maximum adsorption capacity. Moreover, we show that the same strategy can be applied to model adsorption beyond monolayer coverage. Another advantage of the multi-Langmuir approach is that it yields the contribution of each specific site to the CH_4 adsorption capacity of the MOF at different temperatures.

The different sampling strategies of GCMC simulations with potentials were fit to ab initio results,[26] and the present method requires different approximations in the treatment of nuclear motions. Whereas "ab initio" GCMC uses the true anharmonic potential but neglects zero-point vibrational (ZPV) energies, our ab initio multisite Langmuir approach relies on the harmonic approximation for the potential.

Adsorption energies for the different sites in the multisite Langmuir model can be obtained in different ways. Density functional theory (DFT) can treat both local interactions at the metal cation sites (coordination bonds, electrostatics of the cation−adsorbate interaction) as well as long-range Coulomb interactions in the periodic MOF structures. DFT calculations have been carried out for H_2 and CH_4 binding onto the open cation sites in CPO-27, but quantitative agreement of the energies with experiments has not been achieved.[10,36] One reason for this is the inadequate description of dispersion forces by standard functionals which can be overcome by addition of a semiempirical $1/r^6$ term (DFT+D)[37] or by a van der Waals density functional (vdW-DF).[38,39] For adsorption processes in which dispersion forces dominate [hydrocarbons in zeolites,[40−42] H_2 in MOF-5,[33] CH_4 on MgO(001)][25] or play a major role (CO and CO_2 in MOF CPO-27-Mg, -Ni, and -Zn),[43] a hybrid "MP2:DFT(+D)+ΔCCSD(T)" approach has been used. Here, MP2 stands for second-order Møller−Plesset perturbation theory and CCSD(T) for coupled cluster expansion with single and double substitutions and perturbative treatment of triple substitutions. These hybrid methods yielded significantly more reliable results than the corresponding periodic DFT(+D) method alone and also more reliable results than the corresponding MP2+ΔCCSD(T) calculations on finite-size models alone.[40−42]

In this study all interaction energies are calculated with the hybrid MP2(finite model):DFT+D(periodic structure) approach[40−42] that describes the full crystal lattice with DFT+D applying periodic boundary conditions and the adsorption site with the wave function-based electron correlation method MP2. All degrees of freedom are taken into account through relaxation of the position of all atoms in the periodic cell together with the cell size changes that occur with increasing adsorbate loading.

Information about surface heterogeneity is obtained from the surface coverage dependence of the isosteric heat of adsorption. The latter is calculated from adsorption isotherms measured or calculated at different temperatures by applying the Clausius−Clapeyron equation. Whereas all classical adsorption models, including Langmuir and BET models, are derived for absolute adsorption, all experimentally measured adsorption isotherms are excess quantities, i.e., refer to the difference between the amount of adsorbate on the surface and the amount of CH_4 molecules that would occupy the same gas volume as occupied by the adsorbate molecules on the surface. We show here that the dependence of the isosteric heat of adsorption on the surface coverage is different if calculated from excess amounts of adsorbate, and consequently, it may lead to wrong judgements about the surface heterogeneity. More important is that the isotherms measured for real materials are well reproduced after conversion of the calculated absolute adsorbed amounts to surface excess amounts and that reliable predictions of the adsorption capacity can be made for ideal materials.

2. MODELS

The frameworks of the CPO-27 series of isostructural compounds are trigonal with one-dimensional hexagonal pores (Figure 1).[18−21] The vertices (intersections) of the pore walls consist of Mg^{2+} ions that are connected via oxygen atoms. These chains are linked to next parallel chains through 2,5-dihydroxyterephthalate anions (dhtp) that form the walls of the channels. The primitive unit cell (puc) includes six Mg^{2+} ions and three linker molecules, corresponding to three Mg_2(dhtp) formula units (see Supporting Information for a figure). The conventional unit cell includes nine formula units and has $R\bar{3}$ symmetry. Cell parameters for the empty MOF and the MOFs with different loadings of CH_4 were determined using the primitive unit cell. These cell parameters were then also applied for the calculations using the conventional cell.

For CPO-27-Mg two different CH_4 adsorption sites have been identified by neutron diffraction: the Mg^{2+} ion and the linker sites.[10] These sites will be referred to as Mg^{2+} and L sites, respectively. In addition, in the pore there is room for the third adsorption site that is located on top of the Mg^{2+} and L sites and, thus, is denoted as second layer (second L) site. In the primitive unit cell there are six sites of each type (Mg^{2+}, L, and second L) sites, and in the conventional cell there are three times as many.

For the Mg^{2+} and L sites, finite-size models, named **6B**, were cut out from a conventional unit cell that was doubled in the *c* direction and, thus, consist of six consecutive Mg^{2+} cations and of six benzene rings (Figure 1c). For adsorption on the Mg^{2+} site, the CH_4 molecule marked in "yellow" is not present, and it

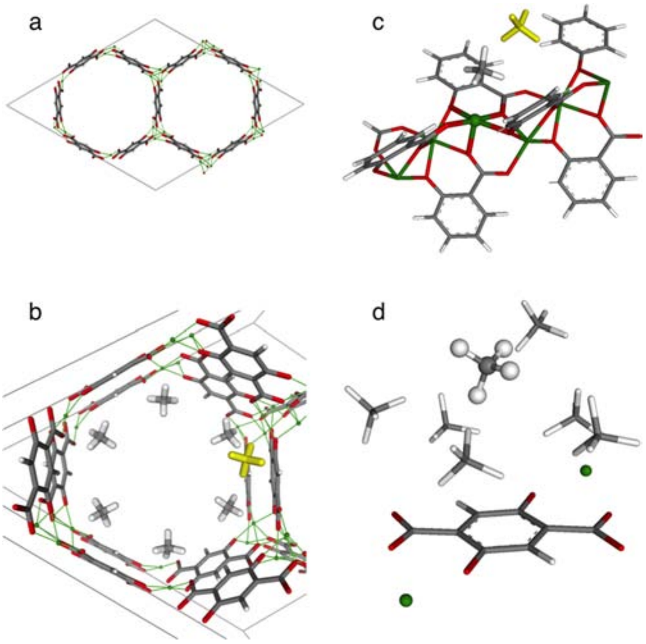

Figure 1. (a) Conventional unit cell of CPO-27-Mg viewed along the *c* direction, (b) part of the MOF with six CH_4 molecules at Mg^{2+} sites and one (yellow) at a linker site, (c) model system **6B** with one CH_4 molecule on a Mg^{2+} site and a second one (yellow) that the linker site, (d) **Mg_2dhtp** model adopted for MP2 calculations. CH_4 in ball and stick style is for second layer site, while CH_4 molecules in stick style belong to the monolayer (Mg^{2+} and L sites).

is the “grey” CH_4 molecule in Figure 1c that is adsorbed. For adsorption on the L site, the “grey” CH_4 molecule is always present, and it is the “yellow” CH_4 molecule that is adsorbed. Figure 1d shows the **Mg_2dhtp** model for the second layer site.

3. METHODS

3.1. Quantum Chemical Calculation of Structures and Energies. The DFT+dispersion calculations with periodic boundary conditions used the VASP program package[44,45] that was modified[46] to include the semiempirical damped $1/r^6$ term for dispersion as suggested by Grimme.[37] For O, C, and H the original dispersion parameters[37] were used, whereas for Mg^{2+} the C_6 and r_0 parameters for Ne were employed.[25] The Perdew−Burke−Ernzerhofer (PBE) exchange−correlation functional was employed. The primitive cell parameters were obtained from calculations of the stress tensor relaxing the ion positions together with the cell size and shape. This was done for the empty MOF and for each MOF structure loaded with different numbers (from one to six, twelve, and eighteen) of CH_4 molecules per unit cell. For the Brillouin zone sampling a $1 \times 1 \times 1$Monkhorst−Pack *k*-point mesh[47] was used. For cell optimizations the valence electrons were described by a plane wave basis set with a kinetic energy cutoff of 800 eV, the core electrons by projector augmented waves. For Mg a small core was used, i.e., the $2p^63s^2$ electrons were included in the valence state. Then the ion positions were reoptimised (keeping the cell constants fixed), and frequencies were calculated using a kinetic energy cutoff of 500 eV.

MP2 calculations were performed with the ricc2 module[48,49] of the TURBOMOLE V6.1 program package,[50] whereas for CCSD(T) calculations, version 6.3 was used.[51] For Mg^{2+}, the frozen core included the 1s electrons only, whereas for other elements only the valence shell electrons were correlated. The resolution of identity (RI) approximation (also known as density fitting) was employed.[52] Dunning’s correlation-consistent aug-cc-pVTZ basis sets[53,54] were applied with appropriate auxiliary basis functions for RI calculations.[55−57] The calculated adsorption energies are corrected for basis set superposition error (BSSE) by the counterpoise scheme.[58] BSSE-corrected MP2 adsorption energies calculated with aug-cc-pVDZ and aug-cc-pVTZ basis sets were extrapolated to the complete basis set limit, denoted cbs(D,T) or, in short, cbs. For the Hartree−Fock (HF) contribution to the MP2 adsorption energy an exponential scheme[59,60] is chosen, whereas an inverse power law[61] is applied to the correlation energy.

As the first step, the interaction energy, ΔE_{ads}, between adsorbed CH_4 and the framework is determined. To ensure that all neighboring adsorption sites are empty and there are no lateral interactions, a conventional unit cell that was doubled in the *c* direction and featured only one CH_4 molecule at one of 36 Mg^{2+} sites when structure optimizations with PBE+D under periodic boundary conditions were made. The adsorption energy for CH_4 on the L site is obtained as an energy change for addition of a second CH_4 molecule to the system that already contains one CH_4 molecule at the closest Mg^{2+} site, with both structures optimized. Then finite-sized models were cut out from these structures (Figure 1c) for which MP2 and DFT+D energies were calculated. These model systems, named **6B**, have a double length of the conventional unit cell in the *c* direction, thus, it consists of six consecutive Mg^{2+} cations and of six benzene rings.

For the second layer sites the adsorption energy is taken as the reaction energy for adding one CH_4 molecule to the full monolayer. The model system for MP2 in this case consists of the one formula unit of CPO-27, **Mg_2dhtp**, and six CH_4 located on Mg^{2+} and L sites (Figure 1d).

The hybrid MP2:PBE+D adsorption energy, $\Delta E_{ads}^{MP2:PBE+D}$, was obtained according to

$$\Delta E_{ads}^{MP2:PBE+D} = \Delta E_{ads}^{pbcPBE+D}(S) + \Delta E_{ads}^{hlcorr}(C) \tag{1a}$$

$$\Delta E_{ads}^{hlcorr}(C) = \Delta E_{ads}^{MP2}(C) - \Delta E_{ads}^{PBE+D}(C) \tag{1b}$$

where $\Delta E_{ads}^{pbcPBE+D}$ (S) is the adsorption energy calculated with PBE+D under periodic boundary conditions (pbc) for the full periodic structure (S) and ΔE_{ads}^{MP2} (C) and ΔE_{ads}^{MPE+D} (C) are adsorption energies for finite-sized model systems C calculated by MP2 and PBE+D, respectively.

Alternatively, the hybrid MP2:PBE+D energy can be written as

$$\Delta E_{ads}^{MP2:PBE+D} = \Delta E_{ads}^{MP2}(C) + \Delta E_{ads}^{LR}(S, C) \tag{1c}$$

with the long-range correction to the MP2 cluster energy defined as

$$\Delta E_{ads}^{LR}(S, C) = \Delta E_{ads}^{pbcPBE+D}(S) - \Delta E_{ads}^{PBE+D}(C) \tag{1d}$$

The final estimate for adsorption energy:

$$\Delta E_{ads}^{final} = \Delta E_{ads}^{MP2:PBE+D} + \Delta E_{ads}^{\Delta CCSD(T)} \tag{1e}$$

also includes higher order correlation effects that are estimated as ΔCCSD(T)/cbs(D,T) = CCSD(T)/cbs(D,T) − MP2/cbs(D,T) for smaller models and added to the MP2/cbs(D,T):PBE+D adsorption energy.

3.2. Adsorption Isotherms. The multisite Langmuir equation is applied which yields the total surface coverage, θ, as the sum of CH_4 adsorbed on different sites:

$$\Theta = \frac{\sum_{site} n_{site}^{a}}{s \cdot n_{max}} = \sum_{site} \frac{K_{site}P}{1 + K_{site}P} \tag{2}$$

n_{site}^{a} and n_{max} are the absolute amount of CH_4 on the surface at a given pressure and maximum amount of CH_4 possible to adsorb on all the sites considered, respectively, which include Mg^{2+}, L, and second L sites. All calculations were done for the “fully activated” ideal structures in which all adsorption sites are assumed to be accessible. Since in “real” samples not all sites are always accessible, e.g., for CH_4 adsorption in CPO-27-Mg only 78% of the sites are accessible,[11] for comparison with observed isotherms the number of available sites is scaled down using a global scaling factor *s*.

The adsorption equilibrium constant for each site is

$$K_{\mathrm{site}} = \frac{Q^{\mathrm{surf}}}{Q^{\mathrm{gas}}} \mathrm{e}^{-\frac{D_0 + E_{\mathrm{lat}}^{\mathrm{site}}}{RT}} \tag{3}$$

where Q^{surf} and Q^{gas} are the partition functions of methane on the surface and in gas phase, respectively. D_0 is the interaction energy between methane and the MOF surface at 0 K, i.e., including the zero-point energy changes, ΔE_{ZPV}:

$$D_0 = \Delta E_{\mathrm{ads}}^{\mathrm{final}} + \Delta E_{\mathrm{ZPV}} \tag{4}$$

According to the Bragg−Williams model[34,35] the lateral interaction energies between adsorbed molecules, E_{lat}, are added to the adsorption energy as a function of coverage and number of nearest neighbors. Thus, for Mg^{2+}, L, and second layer sites, the E_{lat} terms in eq 3 are

$$E_{\mathrm{lat}}^{\mathrm{Mg}} = \frac{1}{2} E^{\mathrm{Mg-Mg}} N^{\mathrm{Mg-Mg}} \Theta_{\mathrm{Mg}} + \frac{1}{2} E_{\mathrm{av}}^{\mathrm{Mg-L}} N^{\mathrm{Mg-L}} \Theta_{\mathrm{L}} \tag{5}$$

$$E_{\mathrm{lat}}^{\mathrm{L}} = \frac{1}{2} E^{\mathrm{L-L}} N^{\mathrm{L-L}} \Theta_{\mathrm{L}} + \frac{1}{2} E_{\mathrm{av}}^{\mathrm{Mg-L}} N^{\mathrm{Mg-L}} \Theta_{\mathrm{Mg}} \tag{6}$$

$$E_{\mathrm{lat}}^{\mathrm{2ndlayer}} = \frac{1}{2} E^{\mathrm{2ndlayer-2ndlayer}} N^{\mathrm{2ndlayer-2ndlayer}} \Theta_{\mathrm{2ndlayer}} \tag{7}$$

where $E^{\mathrm{site-site}}$ is the interaction energies between CH_4 molecules adsorbed at the closest Mg^{2+} or L sites only. For calculating $E^{\mathrm{site-site}}$, a pair of CH_4 molecules is cut from the optimized periodic structure with full monolayer coverage, and the adsorbate−adsorbate interaction is calculated for that methane dimer by CCSD(T)/cbs(D,T) for the fixed periodic PBE+D structure. $N^{\mathrm{site-site}}$ is the number of neighboring adsorbed CH_4 molecules ($N^{\mathrm{Mg-Mg}} = N^{\mathrm{L-L}} = 2$; $N^{\mathrm{2ndlayer-2ndlayer}} = 4$), and Θ_{site} is the coverage of respective site. The interaction energy between CH_4 molecules adsorbed at Mg^{2+} and L sites, $E_{\mathrm{av}}^{\mathrm{Mg-L}}$, is calculated as the average of dimer formation energies of the two ($N^{\mathrm{Mg-L}} = 2$) different pairs of CH_4 molecules at these sites (the adsorption energy for L site includes the interaction energy between CH_4 molecules closest to each other at the Mg^{2+} and L sites).

Since we need the site coverage that we are going to calculate for the determination of the lateral interaction, a self-consistent algorithm is used. We calculate first site coverages without taking into account lateral interactions and then calculate them twice again, but taking the surface coverages obtained in previous step as an input.

The adsorption enthalpy, $\Delta H_{\mathrm{ads}}(T)$, and the heat of adsorption, q_{ads}, at a given temperature T for different types of isolated adsorption sites are calculated as

$$\Delta H_{\mathrm{ads}}(T) = -q_{\mathrm{ads}} = D_0 + \Delta E_{\mathrm{therm}} - RT \tag{8}$$

where RT replaces the volume work and $\Delta E_{\mathrm{therm}}$ is the change of the thermal energy upon adsorption. For the gas

$$E_{\mathrm{therm}}^{\mathrm{gas}} = E_{\mathrm{vib}} + E_{\mathrm{rot}} + E_{\mathrm{trans}} \tag{9}$$

For the solid phase holds

$$E_{\mathrm{therm}}^{\mathrm{solid}} = E_{\mathrm{vib}} \tag{10}$$

The isosteric heat of adsorption, q_{st}, defined as negative of the differential adsorption enthalpy at constant temperature and constant surface coverage, is calculated for 179 and 283 K by numerical differentiation according to

$$q_{\mathrm{st}} = \frac{\partial \Delta H_{\mathrm{ads}} / \partial P}{\partial n / \partial P} = \frac{d/dP \sum_{\mathrm{site}} [\Delta H_{\mathrm{ads}}^{\mathrm{site}} + E_{\mathrm{lat}}^{\mathrm{site}}(P)] \cdot \Theta^{\mathrm{site}}(P)}{d/dP \sum_{\mathrm{site}} \Theta^{\mathrm{site}}(P)} \tag{11}$$

where $\Delta H_{\mathrm{ads}}^{\mathrm{site}}$, $E_{\mathrm{lat}}^{\mathrm{site}}$, and Θ^{site} are calculated according to eqs 2 and 5−8, respectively.

To calculate excess adsorption isotherms we need excess surface amounts, n^{σ}. They are defined as the difference between the absolute amount of CH_4 on the surface, n^{a}, found according to eq 2, and the amount n^{g} of CH_4 contained in a gas of the same volume, $V_{\mathrm{m}}^{\mathrm{a}} n^{\mathrm{a}}$, as the adsorbate occupies on the surface:

$$n^{\mathrm{g}} = \frac{P V_{\mathrm{m}}^{\mathrm{a}} n^{\mathrm{a}}}{RTZ} \tag{12}$$

$$n^{\sigma} = n^{\mathrm{a}} - n^{\mathrm{g}} = \left(1 - \frac{V_{\mathrm{m}}^{\mathrm{a}}}{V_{\mathrm{m}} Z}\right) \cdot n^{\mathrm{a}} \tag{13}$$

where $V_{\mathrm{m}}^{\mathrm{a}}$ is the excluded molar volume of adsorbed methane (80.7 cm^3/mol) calculated from the average distance between CH_4 molecules at Mg^{2+} and L sites (see Supporting Information), V_{m} is the molar volume of methane gas, and Z is compressibility factor calculated according to the Redlich−Kwong equation of state to correct the nonideal behavior of CH_4 in the gas phase at high pressures and low temperatures.

4. RESULTS AND DISCUSSION

4.1. Structures and Vibrational Properties. For the empty CPO-27-Mg framework the cell parameters obtained by PBE+D for the conventional unit cell, $a = b = 2607.9$ and $c = 688.9$ pm, are in good agreement with experimentally determined lattice constants[10,21,36] $a = b = 2588.1, ..., 2602.6$ and $c = 675.87, ..., 687.89$ pm and those previously obtained with the B3LYP+D* functional, $a = b = 2621.2$ and $c = 693.2$ pm.[62] With increasing loading from the empty cell to full monolayer coverage (36 CH_4 molecules in the conventional cell = 12 CH_4 per puc), the lattice constants a and b decrease by 10.4 pm, while there is a slight increase (2.5 pm) of the unit cell in c direction. Consequently, the cell volume stays virtually unchanged. Such cell size changes with increasing CH_4 loading in CPO-27-Mg are also observed with neutron powder diffraction experiments.[10]

The exact position of the adsorbed CH_4 molecules in CPO-27 also depends on the loading: For one CH_4 per puc, the distance between CH_4 and Mg^{2+} is 276.5 pm. When CH_4 is adsorbed on all Mg^{2+} ions (six CH_4 per puc), the C Mg distance increases to 278.8 pm, and after occupation of all L sites (full monolayer coverage), CH_4 is 280.7 pm away from the Mg^{2+} ions. Moreover, the presence of CH_4 on L sites causes the CH_4 on Mg^{2+} sites to move about 15 pm in c direction.

The interaction of CH_4 with the adsorption site and the interaction between adsorbed CH_4 molecules change the C−H bond lengths and vibrational frequencies of methane compared to the gas phase (Table 1). Adsorption breaks the T_d symmetry and, thus, the symmetric C−H stretching vibration (ν_1), which is not IR active in the gas phase, becomes visible and the

Table 1. C−H Stretching Vibrational Frequency Shifts for CH_4 Adsorbed on Mg^{2+} and L Sites Relative to the Gas Phase[a], $\Delta\nu$ (cm^{-1}), Calculated by PBE+D for Different Loadings

site	loading[b]	$\Delta\nu_1$ (symm)[c]	$\Delta\nu_3$ (asymm)[c]		
Mg^{2+}	**1**/0/0	−15	−20	−5	2
	6/0/0	−16	−20	−7	−1
	1/1/0	−15	−17	−12	8
	6/6/0	−17	−21	−14	6
	6/6/6	−12	−15		15
linker	1/**1**/0	−3	−5	−2	1
	3/**3**/0	−3 to −6	−5 to −7	−2 to −4	1 to −2
	6/**6**/0	−6	−7	−4	−3 to −4

[a] Calculated frequencies for symmetric and asymmetric C−H vibrations for free CH_4 are 2946.7 and 3073.7, respectively. [b] Numbers of CH_4 molecules adsorbed on Mg^{2+}/L/second layer sites per primitive unit cell. [c] Symmetric and asymmetric C−H vibrations.

Table 2. Methane Adsorption Energies (in kJ/mol) Calculated with Different Methods on Periodic PBE+D Structures and Model Systems Cut out from These Periodic PBE+D Structures[a]

	Mg^{2+} site			L site			second layer		
	6B[b]	pbc[c]	LR[d]	**6B**[e]	pbc[c]	LR[d]	**Mg_2dhtp**[f]	pbc[c]	LR[d]
PBE+D/pw	−27.1	−27.1	0.0	−12.8	−18.0	−5.2	−14.6	−17.7	−3.1
PBE//PBE+D	−3.3	−2.3	1.0	4.1	1.2	−2.9	2.2	4.6	−2.4
D//PBE+D	−23.9	−24.8	−1.1	−16.9	−19.2	−2.3	−16.8	−22.3	−5.4
MP2/cbs//PBE+D	−28.3			−14.1			−10.8		
ΔE^{hlcorr}	−1.2			−1.3			3.8		
ΔCCSD(T)/cbs	0.5[g]			1.0[g]			−1.2		
final[h]	−27.8			−18.3			−15.1		

[a] MP2 and CCSD(T) energies are corrected for BSSE. [b] see Figure 1c without the "yellow" L site CH_4 molecule. [c] periodic boundary conditions. [d] Long-range correction defined in eq 1d. [e] See Figure 1c, the L site CH_4 molecule is the "yellow" one. The binding energy for the L site is calculated in the presence of one Mg^{2+} site CH_4 molecule (gray in Figure 1c). [f] With six additional CH_4 molecules, see Figure 1d [g] See Table 3, Figure 2 [h] Hybrid (MP2/cbs:PBE+D)+ΔCCSD(T)/cbs//PBE+D

Table 3. CP-Corrected CH_4 Adsorption Energies (kJ/mol) for the Model Systems in Figures 1 and 2[a]

site	model	PBE+D	PBE	D	MP2	CCSD(T)	Δ[b]
Mg^{2+}	**6B**[c]	−27.1	−3.3	−23.9	−28.3		
	0B + M2A + M2B[d]	−23.1	0.2	−23.2	−22.1	−21.6	0.5
	M2A + M2B[d]	−7.1	4.1	−11.2	−6.3	−4.5	1.9
	0B (M1)[d]	−16.0	−3.9	−12.0	−15.7	−17.1	−1.4
L	**6B**[c]	−12.8	4.1	−16.9	−14.1		
	L1 + L2 + L3[d]	−12.5	1.0	−13.5	−11.4	−10.4	1.0
second layer	**Mg_2dhtp**[c]	−14.6	2.2	−16.8	−10.8		
	$(CH_4)_6$[e]	−15.5	0.1	−15.6	−7.4	−8.6	−1.2

[a] Calculated by MP2 and CCSD(T) with the aug-cc-pV(D,T)Z basis set extrapolation at the PBE+D structure. [b] CCSD(T)-MP2. [c] See Figure 1. [d] See Figure 2. [e] Pairwise interaction between the 6 CH_4 molecules in the monolayer, see Figure 1d.

asymmetric C−H stretching vibration (ν_3) looses its three-fold degeneracy. For the full monolayer, coverage the ν_1 vibration is shifted by −17 and −6 cm^{-1} for the Mg^{2+} and L sites, respectively. Each of these asymmetric C−H stretching frequencies of CH_4 which are degenerate in the gas phase has different shifts upon adsorption. For the CH_4 at Mg^{2+} sites the largest shift is −21 cm^{-1} for the loading of a complete monolayer. The second ν_3 vibration is the most sensitive to coverage changes as the frequency shift almost triples from −5 to −14 cm^{-1} when the surface coverage increases from 1 to 12 CH_4 per puc. The formation of the second layer results in a small blueshift of the C−H stretching frequencies of CH_4 adsorbed on Mg^{2+} sites.

Analysis of vibrational frequencies calculated for CPO-27-Mg loaded with increasing amounts of CH_4 reveals that some of the low-frequency modes (below 150 cm^{-1}) are significantly changed with increasing coverage. First, the lowest vibrational mode of the CPO-27-Mg framework (motion of chains of Mg^{2+} ions and linkers) decreases from 51 cm^{-1} for the empty MOF to 23 cm^{-1} for the MOF loaded with 12 CH_4 molecules per puc, six on Mg^{2+} ion, and six on L sites. In this vibration the adsorbed CH_4 molecules are moving together with the framework, and thus, as the vibrating mass increases, the wavenumber of this motion decreases. There are some other framework vibrations that couple with CH_4 vibrations, but they have less influence on adsorption properties.

Upon adsorption the three translational and three rotational degrees of freedom of the CH_4 molecule in the gas phase are converted into six low-frequency vibrations of the CH_4 molecule relative to the adsorption site. The second group of low-frequency modes with significant wavenumber changes is associated with these vibrations. For example, at the loading of one CH_4 per puc, CH_4 vibrates parallel to the surface with a wavenumber of 57 cm^{-1} and the lowest wavenumber that corresponds to a hindered rotation of CH_4 is 77 cm^{-1}. The wavenumber of these modes is shifted to 42 and 66 cm^{-1}, respectively, when two CH_4 molecules more are adsorbed on nearby Mg^{2+} sites. At full coverage of Mg^{2+} sites and half coverage of the L sites (9 CH_4/puc) these frequencies are further shifted to 46 and 54 cm^{-1}, respectively. There are two main factors behind the dependence of these low-frequency modes on surface coverage. First, with increasing surface coverage molecules bind to unoccupied sites next to a molecule already present on the surface. This changes the local environment in which the adsorbed molecules vibrate, and consequently, as the local PES is changed, the vibrational frequencies are shifted. For example, around the minimum the PBE+D potential for the rotation of CH_4 on the Mg^{2+} site along the normal mode for the loadings of one and six molecules/puc is very flat. For a 15° rotation <0.5 kJ/mol is needed (ZPE for this mode is 0.46 kJ/mol for one CH_4/puc). As mentioned before, the lateral interaction energy for the CH_4 on neighboring Mg^{2+} sites is very small (−0.5 kJ/mol), but still there are considerable changes in PES that bring about a shift of −19 cm^{-1} in the corresponding harmonic vibrational frequencies.

In addition, the low-vibrational modes of adsorbed CH_4 are shifted also due to the dynamics, i.e., at higher loadings these vibrations are strongly coupled which increases the vibrating masses and, thus, changes the wavenumbers of these vibrations. For example, at full monolayer coverage the wavenumbers for the vibrations of the six CH_4 molecules parallel to the surface are between 68 and 72 cm^{-1}.

4.2. Adsorption Energies for Individual Sites. Table 2 shows that PBE+D adsorption energies calculated on periodic structures and finite size model systems are the same for the Mg^{2+} site (long-range correction =0.0 kJ/mol) which implies that the **6B** model adopted (Figure 1c) is sufficiently large to include all relevant long-range effects. This is not the case for the L and second layer site models for which long-range corrections of −5.2 and −3.1 kJ/mol have been calculated (Table 2). The major part of the CH_4 adsorption energy of −27.1 kJ/mol for the Mg^{2+} site (PBE+D) is due to dispersion (−24.8 kJ/mol), whereas the PBE share which is due to electrostatic effects (octupole moment and polarizability of CH_4) is only weakly attractive (−2.3 kJ/mol). For the L and second layer sites dispersion dominates even more and the PBE result without dispersion at the PBE+D equilibrium distance is repulsive, +1.2 and +4.6 kJ/mol, respectively).

The reliability of the PBE+D adsorption energies is assessed by comparison with MP2 results for the finite-size model systems cut from the periodic structure (Figure 1), i.e., by evaluating the high-level corrections, eq 1b. Table 2 shows that the latter is only −1.2 and −1.3 kJ/mol for the Mg^{2+} and L sites, respectively.

Estimates of higher order electron correlation effects are based on CCSD(T)/cbs(D,T) calculations on smaller models for the Mg^{2+} ion and the L sites (Table 3 and Figure 2). For the interaction of CH_4 with the Mg^{2+} cation, the **0B** model consisting of three Mg^{2+} cations, two formate anions, and four hydroxide ions is adopted, for which the MP2 binding energy is 1.4 kJ/mol smaller than the CCSD(T) result. On the contrary, MP2 overestimates by 1.9 kJ/mol the interaction between CH_4 and the two closest linkers, calculated for the **M2A** and **M2B** model systems. Each of them includes CH_4 and one of the benzene molecules. Thus, for the Mg^{2+} site the estimated overall difference between CCSD(T) and MP2 adsorption energies is only 0.5 kJ/mol when basis sets augmented with diffuse functions are used. It is important to note that the interaction of CH_4 with the Linkers contributes −4.5 kJ/mol to the CCSD(T)/cbs adsorption energy of −21.7 kJ/mol at the Mg^{2+} site. The Supporting Information reports results for the individual model systems, which show that the MP2 interaction energies calculated for a model system that includes both benzene rings together in one structure, **M2A** ∪ **M2B**, and the sum of the model systems with one benzene molecule, **M2A** + **M2B**, do not differ more than 0.2 kJ/mol. Also, the **0B** + **M2A** + **M2B** sum of the dispersion contribution to PBE+D interaction energies (−23.2 kJ/mol is close to the dispersion part of the **6B** model system (−23.9 kJ/mol), which shows that the additive scheme captures most of the dispersion energy.

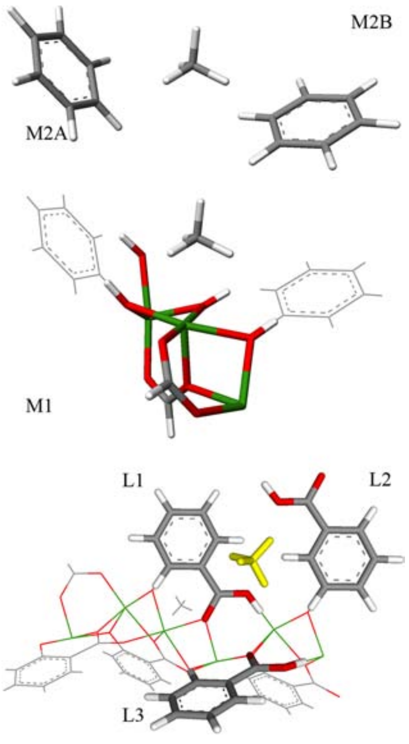

Figure 2. Model systems (in stick style) adopted for CCSD(T) calculations for CH_4 adsorption on the Mg^{2+} and L sites. Model **0B** (M1) consists of three Mg^{2+} cations, two formate anions, and four hydroxide ions. Each of the model systems M2A and M2B consists of one benzene ring and the CH_4 molecule. The M2A ∪ M2B model includes both benzene rings in one structure. Each of the three model systems L1−L3 includes one benzoic acid and one CH_4 molecule in one calculation. The line style CH_4 molecule is the one attached to the Mg^{2+} site (stick style, gray in Figure 1c).

The major part of the adsorption energy for CH_4 on L sites (MP2/cbs = −14.1 kJ/mol) comes from the interaction with linker molecules; the sum of the interaction energies between CH_4 and each of the three closest linker molecules is −11.4 kJ/mol (MP2/cbs), whereas CCSD(T) yields −10.4 kJ/mol. For the second layer site the MP2 and CCSD(T) adsorption energies are estimated by summation of the pairwise interactions between CH_4 at the second layer site and each of the six nearest CH_4 molecules in monolayer (Figure 1D). For each pair, CCSD(T) gives up to 0.3 kJ/mol stronger binding, which leads in total to 1.2 kJ/mol stronger binding than calculated with MP2. The adsorption energy calculated with MP2/cbs when all six CH_4 molecules are present in the monolayer and the sum of the individual pairwise interaction energies yield virtually the same results (−7.5 compared to −7.4 kJ/mol). This is only 3.2 kJ/mol less binding than the −10.8 kJ/mol (Table 2) obtained for the $(CH_4)_6Mg_2$(dhtp) model that includes also a linker molecule (Figure 1d). This shows that CH_4 adsorption beyond a monolayer is controlled by CH_4−CH_4 interactions. Our “best estimates” for the [hybrid MP2/cbs:PBE+D]//PBE+D+ΔCCSD(T) adsorption energies are −27.8, −18.3, and −15.1 kJ/mol for the Mg^{2+}, L, and second layer sites, respectively.

4.3. Lateral Interactions. Lateral interactions affect both the energy and the entropy of adsorption. Table 4 summarizes interaction energies between two CH_4 molecules in the gas phase and when adsorbed at two different sites in CPO-27-Mg. In the gas phase, the CCSD(T)/cbs(D,T) interaction energy calculated at the MP2/aug-cc-pVTZ distance of 364 pm is −2.2 kJ/mol. This is close to the previously calculated[63,64] CCSD(T)/cbs dimerization energies of −2.3 and −2.1 kJ/mol which used two point (X = T, Q) and three point (X = D, T, Q) extrapolations for the same aug-cc-pVXZ basis sets. If all Mg^{2+} sites are occupied (six CH_4 per puc), the distances between CH_4 molecules at neighboring Mg^{2+} sites are 517 and 689 pm in *a* (or *b*) and *c* directions, respectively, and thus, their interaction is weak (−0.5 kJ/mol for 517 pm, Table 4).

At a loading of 12 CH_4 per puc (two CH_4 per Mg^{2+}), all six L sites are populated in addition to the six Mg^{2+} sites. In this full monolayer each CH_4 at a Mg^{2+} site has three close neighbors at L sites. The distances between these CH_4 molecules are close to the distance in the CH_4 gas phase dimer, and the average

Table 4. Interaction Energies (kJ/mol) and Distances (pm) between Two CH_4 in the Gas Phase and Adsorbed on Mg^{2+} and Nearby L Sites in CPO-27-Mg

		R	ΔE	
gas phase	PBE+D	382.2[a]	−2.76	
			MP2	CCSD(T)
	aug-cc-pVTZ	(382.2)[b]	−1.29	
	cbs (D,T)	(382.2)[b]	−1.48	−1.70
	aug-cc-pVTZ	363.5[a]	−1.89	
	cbs(D,T)	(363.5)[c]	−2.05	−2.23
$Mg^{2+}\cdots$linker	cbs(D,T)	363.0[d]	−1.65	−1.89
		412.7[d]	−1.52	−1.66
		425.3[d]	−1.28	−1.44
linker⋯linker	cbs(D,T)	444.4[d]	−1.01	−1.16
$Mg^{2+}\cdots Mg^{2+}$	cbs(D,T)	517.1[d]	−0.53	−0.55

[a] Optimized. [d] Fixed at the PBE+D optimized structure for a full monolayer coverage of six CH_4 molecules on the six Mg^{2+} sites and of six CH_4 molecules at the six L sites in a primitive unit cell, see Supporting Information for a figure defining the distances. [b] Single point calculation at the PBE+D gas-phase dimer structure. [c] Single point calculation at the MP2/aug-cc-pVTZ gas-phase dimer structure.

interaction energy per pair of CH_4 molecules is −1.7 kJ/mol (Table 4). A CH_4 molecule at an L site also interacts with neighboring CH_4 molecules at two other L sites contributing −1.2 kJ/mol per CH_4 pair.

The additional energy contributions from nearby molecules, $\Delta EL_{\mathrm{at}}^{\mathrm{site}}$, that are used in eq 4 for the calculation of isotherms at maximum loading, according to eqs 5−6, are

$$\Delta E_{\mathrm{lat}}^{\mathrm{Mg}} = \frac{1}{2}(-0.55)\cdot 2 + \frac{1}{2}[(-1.66 - 1.44)/2]\cdot 2$$
$$= -2.1 \text{ kJ/mol}$$

and

$$\Delta E_{\mathrm{lat}}^{\mathrm{L}} = \frac{1}{2}(-1.16)\cdot 2 + \frac{1}{2}[(-1.66 - 1.44)/2]\cdot 2$$
$$= -2.7 \text{ kJ/mol}$$

Hence, in a monolayer, the average lateral interaction energy can be as high as 2.4 kJ/mol, which is 10% of the average adsorption energy for the Mg^{2+} and L sites (−23.2 kJ/mol). Note that the largest lateral interaction between a Mg^{2+} and a linker site in Table 4 (−1.9 kJ/mol) is already included in our definition of the adsorption energy of the linker site, because for its calculation a model is used that includes two CH_4 molecules, one at the linker site and one at the Mg^{2+} site.

4.3. Enthalpies and Entropies of Adsorption.

Table 6 shows the thermodynamic functions for CH_4 adsorption on Mg^{2+}, L, and second layer sites that we will use to calculate the adsorption isotherms. They are obtained for populating all six Mg^{2+} sites/puc, addition of six CH_4 molecules to L sites when all Mg^{2+} sites are occupied, and adsorbing six CH_4 molecules on top of a full monolayer, according to (n = 0−2, respectively)

$$\frac{1}{6}(CH_4)_{6n}/\mathrm{MOF} + CH_4 \rightarrow \frac{1}{6}(CH_4)_{6n+6}/\mathrm{MOF} \tag{14}$$

We note that the ZPV energy changes are about 7, 8, and 17% of the binding energies on the Mg^{2+}, L and second layer sites, respectively. Thus, quantum effects must be taken into account when calculating adsorption enthalpies.

When calculating the vibrational frequencies we use a partial Hessians assuming that the change of the thermodynamic functions is due only to the six intermolecular degrees of freedom for every adsorbed molecule, an approximation that we discuss below. The motions of adsorbed CH_4 relative to the adsorption site can be described as six low-frequency vibrations (also covered by the partial Hessian) or as three vibrations and three (free) rotations if one assumes that upon adsorption the CH_4 on the surface has retained its rotational degrees of freedom. For the H_2 adsorption in MOF-5 we have shown that this has strong influence on adsorption enthalpy and Gibbs free energy,[33] and this is also seen in Table 5. Comparison with experimentally measured isotherms in Figure 7 below reveals that the calculated amount of CH_4 adsorbed in the ideal structures is underestimated when all six CH_4 movements relative to the MOF surface are treated as vibrations.

Quantum dynamic six-dimensional calculations of the coupled translation−rotation eigenstates of CH_4 confined in clathrate hydrate by Matanovic et al.[65] show that the rotational energy levels of physically adsorbed CH_4 are very similar to those of the gas phase. In other words, the $(2j + 1)^2$ degeneracy of the rotational energy levels of CH_4 in the gas phase with the quantum number j is preserved also in the adsorbed state, but because of the angular anisotropy of the PES (rotational barriers) the energy levels are shifted and split into (possibly degenerate) sublevels. Energy levels calculated with the harmonic oscillator model for hindered rotations do not have this degeneracy, and thus, the entropy loss upon adsorption is overestimated. Therefore, the use of the gas-phase rotational partition function for the adsorbed CH_4 instead of harmonic oscillator partition functions gives better agreement with measured isotherms (Figure 7).

The Supporting Information provides additional insight into this problem by solving the Schrödinger equation for a one-

Table 5. Adsorption Enthalpies, ΔH, Change in ZPV Energies upon Adsorption of CH_4, ΔE_{ZPE}, Thermal Energy Change, $\Delta E_{\mathrm{therm}}$, and Adsorption Entropy Term, $T\Delta S$ (all in kJ/mol) Calculated for Different Adsorption Sites Using the Hybrid MP2:PBE+D+ΔCCSD(T)//PBE+D Method

		adsorbed CH_4 has 3 rotational and 3 vibrational degrees of freedom				adsorbed CH_4 has 6 vibrational degrees of freedom			
		ΔH	ΔE_{ZPE}	$\Delta E_{\mathrm{therm}}$	$T\Delta S$	ΔH	ΔE_{ZPE}	$\Delta E_{\mathrm{therm}}$	$T\Delta S$
179 K	Mg^{2+}	−26.7	2.0	0.6	−18.5	−24.1	4.2	1.0	−19.8
	linker	−17.5	1.4	0.9	−17.1	−14.9	3.6	1.3	−18.6
	second layer	−13.6	2.6	0.4	−18.6	−10.8	5.2	0.6	−20.1
298 K	Mg^{2+}	−26.4	2.0	1.9	−30.3	−22.4	4.2	3.7	−30.9
	linker	−17.1	1.4	2.2	−28.0	−13.2	3.6	4.0	−28.8
	second layer	−13.3	2.6	1.7	−30.5	−9.2	5.2	3.1	−31.5

dimensional model potential of the hindered rotation and comparing the results with those obtained for free rotation and a harmonic oscillator description. Thermal energies calculated for adsorbed CH_4 with the more precise hindered rotation approach are larger because more states are populated as a result of the degeneracy of rotational energy levels and because the adsorption potential energy levels are lower. The fact that the calculated isotherms can reproduce experimentally determined excess adsorbed amounts (see below) shows the reliability of Gibbs free energies calculated with the free rotor model. This indicates that the adsorption entropy changes listed in Table 5 may be also overestimated and should be regarded as an upper limit.

The assumption of freely rotating CH_4 on the surface is also supported by IR measurements which show that CH_4 adsorbed in zeolites has retained some of its rotational motion.[66,67] Furthermore, inelastic neutron scattering experiments[68,69] have shown that CH_4−CH_4 interactions lower the barrier to the rotation for CH_4 adsorbed on the MgO (001) surface, and therefore, CH_4 adsorbed also on five coordinated Mg^{2+} ions can be characterized as if CH_4 has retained some of its rotational motion. Additional corroboration for the use of freely rotating adsorbed CH_4 model is provided by calculation of adsorption entropies for alkane adsorption in zeolites for which good agreement with experiment is obtained if mobile physisorption (i.e., free translation and rotation in two dimensions) is assumed.[70]

Table 6. Thermodynamic Functions (kJ/mol per CH_4 molecule) and Equilibrium Constant K (1/atm) for the Simultaneous Adsorption of 1−6 CH_4 Molecules at the 6 Mg^{2+} Sites[a]

n	ΔE_{ZPV}	ΔE_{therm}	ΔH^b	ΔS^c	$-T\Delta S$	ΔG	K
1	2.01	1.73	−26.39	−101.06	28.62	2.23	0.388
2	1.93	1.79	−26.42	−100.07	28.34	1.92	0.443
3	1.90	1.80	−26.43	−99.93	28.30	1.87	0.452
4	1.93	1.78	−26.43	−100.32	28.41	1.98	0.431
5	1.95	1.75	−26.43	−101.09	28.63	2.2	0.392
6	1.97	1.73	−26.43	−101.80	28.83	2.39	0.362
average	1.95	1.76	−26.42	−100.71	28.52	2.10	0.411
max−min	0.11	0.07	0.04	1.87	0.53	0.52	0.090
			Full Hessian				
average	1.80	1.72	−26.63	−100.96	28.59	1.97	0.445
max−min	0.54	0.34	0.34	5.44	1.54	1.77	0.324

[a] At 283.2 K and 1 atm. Lateral interactions are not taken into account; see eq 15. [b] CH_4 is assumed to rotate freely. Partial Hessian is used for frequencies. $\Delta E = -27.8$ kJ/mol for $n = 1-6$, $RT = 2.35$ kJ/mol. [c] J/mol K.

Table 6 shows thermodynamic data for 283.2 K and 1 atm calculated for Mg^{2+} sites only, using frequencies obtained for unit cells with one to six CH_4 molecules occupying the six Mg^{2+} sites in the PUC, i.e., for the reactions (n = 1−6):

$$\frac{1}{n}\text{MOF} + CH_4 \rightarrow \frac{1}{n}(CH_4)_n/\text{MOF} \tag{15}$$

The free rotor model is adopted, i.e., only three of the six relative motions of adsorbed CH_4 are treated as vibrations. Adsorbate−adsorbate interaction energies are ignored, which implies that the binding energies per CH_4 molecules are the same for all six loadings on a given site type. If the assumptions the Langmuir model would be ideally fulfilled, the results should be independent of the loading, i.e., the six calculations should give the same results. If the frequencies are obtained by diagonalization of the full mass weighted Hessian, the ZPV energies show a variation of 0.5 kJ/mol, the entropy contributions to the free energy ($T\Delta S$) a variation of 1.5 kJ/mol ,and the Gibbs free energies a variation of 1.8 kJ/mol. These variations are due to the different relaxation of the framework structure but are also affected by numerical errors on the calculated frequencies. Particularly large are the effects of numerical errors for small wavenumbers.[71] The 10 lowest wavenumbers of empty MOF frameworks are in the 51−134 cm^{-1} range. On CH_4 adsorption these wavenumbers do not change much, and the difference of numerical errors may therefore be as large as the effect itself. It may therefore be a better approximation to assume that the change of the MOF framework structure does not make any contribution and that the change of the thermodynamic functions is due only to the six intermolecular degrees of freedom for every adsorbed molecule. These are the numbers given in the first six rows of Table 6. The spreads of the six values for the thermodynamic functions are now much smaller, 0.1 kJ/mol only for the ZPV energy and 0.5 kJ/mol for both the entropy term and the Gibbs free energy. The average values over the six different loadings, however, are not very different depending on whether the full or the partial Hessian is used. The average values of the zero point energy, the entropy term, and the Gibbs free energy differ only by 0.15, 0.07, and 0.13 kJ/mol, respectively. Working with the partial Hessian we have eliminated a source of numerical error without neglecting a significant physical effect. The thermodynamic functions in Table 5 have been obtained with the partial Hessian, as always in this paper if not otherwise noted. The full Hessian results for the individual loadings are given in the Supporting Information.

The remaining variation in the partial Hessian results for the Gibbs free energy of adsorption (Table 6) shows that, contrary to the Langmuir assumption, the thermodynamic functions are dependent on the surface concentration. The Gibbs free energy reaches a minimum for n = 3 and a maximum for full coverage, n = 6. Consequently, adsorption isotherms calculated using thermodynamical parameters obtained from different CH_4 loadings have different adsorption capacities at a given pressure as illustrated in Figure S4. For this reason, the equilibrium constant for the whole adsorption process becomes dependent on surface coverage.

4.4. Adsorption Isotherms.

Figure 3 shows the amount of CH_4 adsorbed on the different types of sites (Mg^{2+}, L, and second layer sites) as function of pressure. It is clearly seen that the Mg^{2+} site, which is the strongest adsorption site, is populated first. This is the main cause for the rapid increase of the adsorption isotherm at relatively low pressures. Adsorption on the L sites starts at higher pressures. Below the critical temperature of methane[72] (190.6 K) the pressure for the population of Mg^{2+} ion and L sites is sufficiently different to give a rise to the inflection point in the adsorption isotherm when it is ploted in logarithmic scale. Subcritical temperatures monolayer formation is completed at about 2 bar, whereas at supercritical conditions saturation of all adsorption sites, in particularly the L sites, is difficult to reach. For example, at 298 K and 100 bar only 75% of the L sites is occupied.

CH_4 molecules in the second layer interact mainly with the CH_4 molecules in the monolayer, and therefore, the conditions for formation of the second layer are governed by adsorbate−

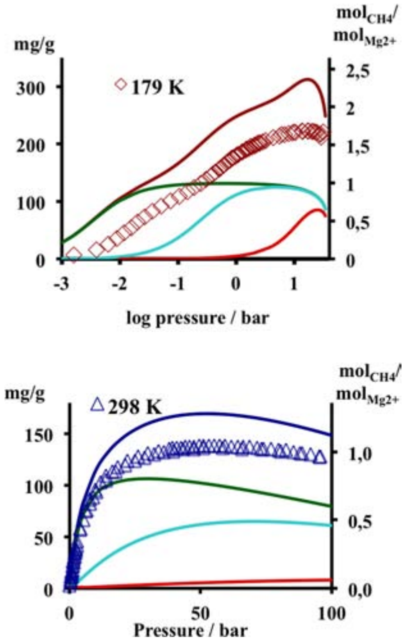

Figure 3. Excess isotherms for the adsorption of CH_4 on Mg^{2+} (green), L (light blue), and second layer (red) sites in ideal CPO-27-Mg at 179 K (up) and 298 K (bottom). Data points are experimentally determined amounts of adsorbed CH_4.[11] For all isotherms it is assumed that CH_4 rotations are preserved in the adsorbed state. The upper figure (179 K) uses logarithmic scale for the pressure.

adsorbate interactions. This is closely related to BET theory, which assumes that all adsorbate layers on top of the monolayer are equal to the liquid state. Moreover, gases can condense by increasing the pressure only below critical temperature, and thus, adsorption can easily proceed beyond monolayer coverage only under subcritical conditions. For example, at 179 K one-third of the second layer sites for the ideal MOF structure is occupied at 7.6 bar, whereas at 298 K a pressure of 349 bar is needed to reach this coverage. This clearly shows that the advantage for gas storage in porous solids at supercritical conditions comes from gas–solid interactions.

Figure 4 shows the effect of the lateral energy contribution for the calculated adsorption isotherms. Adding the adsorbate–adsorbate interaction energies, according to eqs 3, 5, and 6, increases the maximum excess adsorption capacity by about 15%, from 158 to 184 mg/g at 283 K and from 113 to 130 mg/g at 343 K. For the ideal material, maximum excess adsorption capacities are 315, 184, and 130 mg/g or 2.38, 1.39, and, 0.98 mol (CH_4)/mol (Mg^{2+}) at 179, 283, and 343 K, respectively.

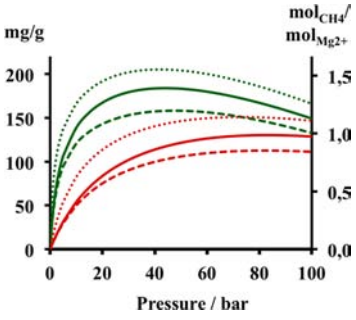

Figure 4. Calculated excess adsorption isotherms (solid lines) for CH_4 adsorption in ideal CPO-27-Mg for two different temperatures: 283 K (green lines) and 343 K (red lines). Dashed lines are isotherms calculated without lateral interactions, solid lines are isotherms for which lateral interaction are calculated according to Bragg–Williams model, and for isotherms represented with dotted lines, the maximum lateral interaction for every site is assumed.

Assuming the maximum lateral interactions for every site instead of the loading dependent contributions according to eqs 5 and 6 yields too large adsorbed amounts as the dotted lines in Figure 4 show.

Figure 5 shows calculated excess and absolute adsorption isotherms for sub- and supercritical temperatures. At relatively low pressures (low surface coverage) both excess and absolute adsorption isotherms are the same because the gas-phase density is negligible relative to the adsorbed phase density. With increasing pressure the real surface coverage increases monotonically, as evidenced by the absolute isotherms, whereas the excess isotherms reach a maximum before all the adsorption sites are occupied. Considering this, it is not possible to apply the Clausius–Clapeyron equation for calculating isosteric heats of adsorption at (around) the maximum of the surface excess isotherms under supercritical conditions.[73−76]

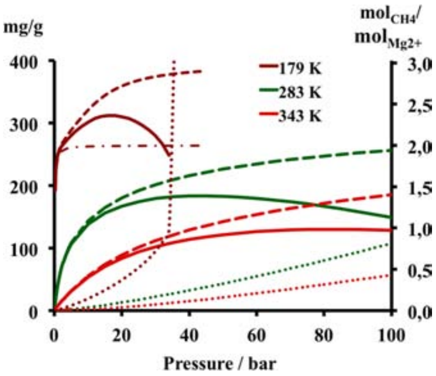

Figure 5. Calculated excess (solid lines) and absolute (dashed lines) adsorption isotherms for CH_4 adsorption in ideal CPO-27-Mg (CH_4 rotations preserved). Dotted lines represent the amount of CH_4 in the gas phase that has the same volume as it occupies on the surface. Dash-dot line is the absolute adsorption isotherm for which formation of the second layer is omitted.

Whereas the absolute adsorbed amount is directly obtained by our multisite Langmuir/Bragg–Williams approach, to determine it experimentally would require to know the exact volume or density of the adsorbed phase. The latter cannot be measured, and it is usually assumed that the density of the adsorbed phase is constant (critical density or density of the liquid) or that the volume of the adsorbed phase it constant and equal to the total pore volume.[74]

For subcritical conditions or low pressures, the difference between excess and absolute isotherms is negligible, and absolute adsorption models can be used. Figure 5 shows that under such conditions (179 K) formation of a full monolayer is completed at relatively low pressures, and when increasing the pressure, further adsorption continues with formation of the next adsorption layers, i.e., pore filling starts.

4.5. Heats of Adsorption as Function of Coverage.

Figure 6 shows that the dependence of the isosteric heat of adsorption on surface coverage is different whether the surface coverage is calculated from absolute (dotted lines) or excess isotherms (solid lines). There is no difference for very low surface coverages. At supercritical conditions (283 K) with

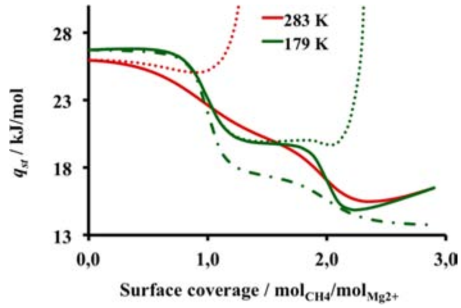

Figure 6. Dependence of the calculated isosteric heats of adsorption, q_{st}, on surface coverage in subcritical (green lines, 179 K) and supercritical (red lines, 283 K) conditions. Continuous and dotted lines correspond to isosteric heats calculated using constant absolute and excess surface coverage, respectively. The dash-dot line represents the isosteric heat of adsorption calculated at 179 K using constant absolute surface coverage without lateral interactions.

increasing loading the isosteric heat of adsorption calculated from constant absolute coverage decreases continuously, whereas for constant excess adsorbed amount the initial decrease of the isosteric heat of adsorption is much smaller and at loadings close to the maximum of the excess adsorption isotherm starts to increase rapidly. Because the slope of the excess adsorption isotherm is zero at its maximum, the isosteric heat of adsorption is not defined at this pressure (eq 11).[74−76] The latter behavior results from the different shapes of the corresponding adsorption isosteres from which isosteric heats of adsorption are calculated. Adsorption isosteres for absolute surface coverage are perfectly linear. Because the excess surface coverage is smaller than the absolute adsorbed amount, to reach the same (apparent) surface coverage, higher pressure is needed for excess isosteres. With temperature increase, progressively higher pressure must be applied which leads to the increase of the slope of the isostere, $\partial \ln P/\partial(1/T)$ at constant loading (see Figure S3) and to an artificial increase of the heat of adsorption at high surface coverage. This is very likely the reason for the increase of the isosteric heats of adsorption with increasing CH_4 coverage that has been measured for MOF-5 and CPO-27-Mg.[10,77]

The isosteric heat of adsorption at certain surface coverage corresponds to the weighted average of adsorption enthalpies of all sites plus the lateral interaction energies. Below the critical temperature (at 179 K in Figure 6), the isosteric heat of adsorption decreases with increasing loading. It shows characteristic steps for filling the different types of adsorption sites with decreasing adsorption enthalpies. Until all Mg^{2+} sites are occupied (coverage of 1.0 in Figure 6) the isosteric heat of adsorption stays constant at the same value as at zero coverage, 26.6 kJ/mol. At higher temperature (283 K), at surface coverage of 0.001 the adsorption enthalpy for the Mg^{2+} site and the isosteric heat of adsorption are −26.4 and −26.0 kJ/mol, respectively. With a further temperature increase from 283 to 343 K, the percentage of occupied Mg^{2+} sites decreases from 94.9 to 90.2%, and the difference between the adsorption enthalpy for the Mg^{2+} site and the isosteric heat of adsorption increases to 0.9 kJ/mol.

Because of the lateral interactions, the second plateau in the isosteric heat of adsorption in Figure 6 is at 20 kJ/mol, about 2.5 kJ/mol higher than the adsorption enthalpy of the L sites at zero coverage (17.5 kJ/mol) or than the isosteric heat of adsorption calculated without the lateral interactions (dash-dot line in Figure 6). When the population of the second layer sites starts to dominate (surface coverage beyond two CH_4 per Mg^{2+}) the isosteric heat of adsorption drops to 15 kJ/mol and then increases with further increase of the surface coverage. The isosteric heat of adsorption calculated without the lateral interactions does not show such an increase. This illustrates that the isosteric heat of adsorption can increase with loading due to adsorbate−adsorbate interactions, but only when weaker adsorption sites are not available.

4.6. Comparison with Experiment. From measured adsorption isotherms at 179 and 283 K, Dietzel et al.[11] inferred a value of 20.5 kJ/mol for the initial isosteric heat of adsorption. From isotherms in the 270−343 K range, both Dietzel et al.[11] and Wu et al.[10] found the initial isosteric heats of adsorption to be close to 18 kJ/mol. Adsorption enthalpies for the Mg^{2+} site calculated using models that treat CH_4 motions relative to surface as vibrations or free rotations (Table 5) and the calculated isosteric heats of adsorption (Figure 6) reproduce that trend but yield too large values most likely due to the underestimation of thermal energies in the free rotor model compared to a proper treatment of hindered rotations.

The adsorption enthalpy for second layer sites, −13.6 kJ/mol at 179 K (Table 5), is very close to the enthalpy of sublimation of solid methane[78] of 10.0 kJ/mol at 89 K and to the enthalpy of vaporization of liquid methane[79] of 8.17 kJ/mol at 111.7 K. This shows again that the adsorption beyond monolayer coverage is determined by interactions between adsorbed methane molecules, and the advantage of a higher adsorption capacity coming from adsorbent−adsorbate interactions influences only the adsorption into the monolayer, i.e., the attractive pore wall potential, is shielded by the monolayer from the additional layers. Therefore, the growth of the second layer follows the increase of the amount of methane in the gas phase at the same conditions.

The adsorption isotherms in Figure 7 calculated for the ideal material overestimate the predicted excess amounts of adsorbed CH_4, but if one assumes that only 78% of the sites in this crystal are available for adsorption, as suggested for this particular material sample,[11] good agreement between experimentally measured and calculated isotherms is reached.

The real volumetric methane storage capacity depends on the amount of material that can be pressed into a given container volume. For the CPO-27 materials, this packing density is reported to be 80−85%.[10] In Figure 7 the volumetric storage capacities are calculated from crystal densities that can be regarded as maximum volumetric storage capacity of ideal crystals, i.e., it is an intrinsic property of the material and independent of sample processing technologies. The maximum excess volumetric storage capacity calculated from the crystal density (0.894 g/cm^{-3}) of the empty MOF at room temperature, 211 cm^3 (STP)/cm^3, exceeds the DOE target by far and reaches as high as 389 cm^3 (STP)/cm^3 at 179 K, while the absolute amounts of adsorbed CH_4 at these condition are 257 and 434 cm^3 (STP)/cm^3.

5. CONCLUSIONS

Lateral interactions between CH_4 molecules adsorbed on different sites in MOF CPO-27-Mg cannot be neglected. Adsorbate−adsorbate interactions contribute about 10% to the average adsorption energy at monolayer coverage and about 15% to the maximum excess adsorption capacity.

Within a multisite Langmuir approach for predicting adsorption isotherms, the Bragg−Williams model provides a

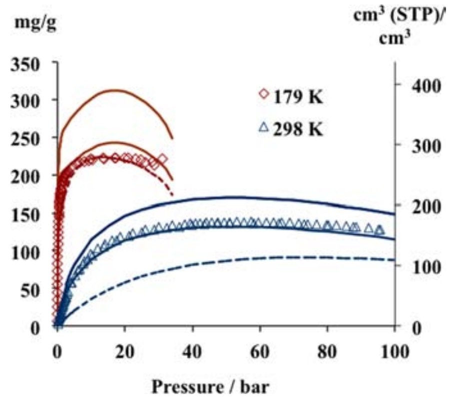

Figure 7. Calculated excess adsorption isotherms for CH_4 adsorption in CPO-27-Mg for which experimentally determined availability (78%) of adsorption sites is assumed (solid lines) and for ideal material (dashed lines). Data points are experimentally determined amounts of adsorbed CH_4.[11] Dotted lines: isotherms for adsorbed CH_4 with six vibrational motions relative to the adsorption sites in ideal material. Solid and dashed lines: calculated isotherm with preserved rotational degrees of freedom of adsorbed CH_4.

suitable means of taking adsorbate−adsorbate interactions into account. In combination with our hybrid MP2/cbs:DFT+D+ΔCCSD(T) approach for calculating adsorption energies with chemical accuracy, reliable ab initio predictions of adsorption isotherms can be made. These predictions have reached a level of accuracy that structural surface models can be tested, i.e., deviations between adsorption isotherms predicted for a perfect crystal and measured isotherms may point to imperfections of the sample, e.g., nonaccessibility of part of the adsorption sites.

Another advantage of ab initio calculated isotherms is that they yield both the excess and the absolute amounts of adsorbed gas. The latter is not easy to measure but necessary to avoid artifacts in determining isosteric heats of adsorption as function of loading.

■ ASSOCIATED CONTENT

Ⓢ Supporting Information

Details of MP2 and CCSD(T) calculations; excess isotherms calculated using the excluded volume; adsorption isosteres calculated for absolute and excess surface coverage of CH_4; and excess isotherms calculated for different sets of vibrational frequencies. This material is available free of charge via the Internet at http://pubs.acs.org.

■ AUTHOR INFORMATION

Corresponding Author

js@chemie.hu-berlin.de

Present Address

[†]Institute of Chemistry, University of Tartu, Ravila 14a, 50411, Tartu, Estonia

Notes

The authors declare no competing financial interest.

■ ACKNOWLEDGMENTS

This work has been funded by the EU within the MOFCAT project under the NMP programme (contract no. NMP4-CT-2006-033335). It has also been supported by German Research Foundation (DFG) within the cluster of excellence UNICAT.

■ REFERENCES

(1) Sun, Y.; Liu, C.; Su, W.; Zhou, Y.; Zhou, L. *Adsorption* **2009**, *15*, 133−137.

(2) Düren, T.; Sarkisov, L.; Yaghi, O. M.; Snurr, R. Q. *Langmuir* **2004**, *20*, 2683−2689.

(3) Chae, H. K.; Siberio-Perez, D. Y.; Kim, J.; Go, Y.; Eddaoudi, M.; Matzger, A. J.; O'Keeffe, M.; Yaghi, O. M. *Nature* **2004**, *427*, 523−527.

(4) Ferey, G.; Mellot-Draznieks, C.; Serre, C.; Millange, F.; Dutour, J.; Surble, S.; Margiolaki, I. *Science* **2005**, *209*, 2040−2042.

(5) Farha, O. K.; Yazaydın, A. Ö.; Eryazici, I.; Malliakas, C. D.; Hauser, B. G.; Kanatzidis, M. G.; Nguyen, S. T.; Snurr, R. Q.; Hupp, J. T. *Nat. Chem.* **2010**, *2*, 944−948.

(6) Furukawa, H.; Ko, N.; Go, Y. B.; Aratani, N.; Choi, S. B.; Choi, E.; Yazaydin, A. Ö.; Snurr, R. Q.; O'Keeffe, M.; Kim, J.; Yaghi, O. M. *Science* **2010**, *329*, 424−428.

(7) Eddaoudi, M.; Kim, J.; Rosi, N.; Vodak, D.; Wachter, J.; O'Keeffe, M.; Yaghi, O. M. *Science* **2002**, *295*, 469−472.

(8) Bourrelly, S.; Llewellyn, P. L.; Serre, C.; Millange, F.; Loiseau, T.; Ferey, G. *J. Am. Chem. Soc.* **2005**, *127*, 13519−13521.

(9) Ma, S.; Sun, D.; Simmons, J. M.; Collier, C. D.; Yuan, D.; Zhou, H.-C. *J. Am. Chem. Soc.* **2008**, *130*, 1012−1016.

(10) Wu, H.; Zhou, W.; Yildirim, T. *J. Am. Chem. Soc.* **2009**, *131*, 4995−5000.

(11) Dietzel, P. D. C.; Besikiotis, V.; Blom, R. *J. Mater. Chem.* **2009**, *19*, 7362−7370.

(12) Wang, X.-S.; Ma, S.; Rauch, K.; Simmons, J. M.; Yuan, D.; Wang, X.; Yildirim, T.; Cole, W. C.; López, J. J.; Meijere, A. d.; Zhou, H.-C. *Chem. Mater.* **2008**, *20*, 3145−3152.

(13) Llewellyn, P. L.; Bourrelly, S.; Serre, C.; Vimont, A.; Daturi, M.; Hamon, L.; Weireld, G. D.; Chang, J.-S.; Hong, D.-Y.; Hwang, Y. K.; Jhung, S. H.; Ferey, G. *Langmuir* **2008**, *24*, 7245−7250.

(14) Seki, K. *Chem. Commun.* **2001**, 1496−1497.

(15) Senkovska, I.; Kaskel, S. *Microporous Mesoporous Mater.* **2008**, *112*, 108−115.

(16) Wang, H.; Getzschmann, J.; Senkovska, I.; Kaskel, S. *Microporous Mesoporous Mater.* **2008**, *116*, 653−657.

(17) Getzschmann, J.; Senkovska, I.; Wallacher, D.; Tovar, M.; Fairen-Jimenez, D.; Düren, T.; Baten, J. M. v.; Krishna, R.; Kaskel, S. *Microporous Mesoporous Mater.* **2010**, *136*, 50−58.

(18) Rosi, N. L.; Kim, J.; Eddaoudi, M.; Chen, B.; O'Keeffe, M.; Yaghi, O. M. *J. Am. Chem. Soc.* **2005**, *127*, 1504−1518.

(19) Dietzel, P. D. C.; Panella, B.; Hirscher, M.; Blom, R.; Fjellvåg, H. *Chem. Commun.* **2006**, 959−961.

(20) Dietzel, P. D. C.; Morita, Y.; Blom, R.; Fjellvåg, H. *Angew. Chem., Int. Ed.* **2005**, *44*, 6354−6358.

(21) Dietzel, P. D. C.; Blom, R.; Fjellvåg, H. *Eur. J. Inorg. Chem.* **2008**, 3624−3632.

(22) Getman, R. B.; Bae, Y.-S.; Wilmer, C. E.; Snurr, R. Q. *Chem. Rev.* **2012**, *112*, 703−723.

(23) Chavan, S.; Vitillo, J. G.; Groppo, E.; Bonino, F.; Lamberti, C.; Dietzel, P. D. C.; Bordiga, S. *J. Phys. Chem. C* **2009**, *113*, 3292−3299.

(24) Caskey, S. R.; Wong-Foy, A. G.; Matzger, A. J. *J. Am. Chem. Soc.* **2008**, *130*, 10870−10871.

(25) Tosoni, S.; Sauer, J. *Phys. Chem. Chem. Phys.* **2010**, *12*, 14330−14340.

(26) Dzubak, A. L.; Lin, L.-C.; Kim, J.; Swisher, J. A.; Poloni, R.; Maximoff, S. N.; Smit, B.; Gagliardi, L. *Nat. Chem.* **2012**, DOI: 10.1038/NCHEM.1432.

(27) Tafipolsky, M.; Schmid, R. *J. Phys. Chem. B* **2009**, *113*, 1341−1352.

(28) Tafipolsky, M.; Amirjalayer, S.; Schmid, R. *J. Phys. Chem. C* **2010**, *114*, 14402−14409.

(29) Salles, F.; Ghoufi, A.; Maurin, G.; Bell, R. G.; Mellot-Draznieks, C.; Ferey, G. *Angew. Chem., Int. Ed.* **2008**, *47*, 8487−8491.

(30) Huang, B. L.; McGaughey, A. J. H.; Kaviany, M. *Int. J. Heat Mass Transfer* **2007**, *50*, 393−404.

(31) Düren, T.; Baeb, Y.-S.; Snurr, R. Q. *Chem. Soc. Rev.* **2009**, *38*, 1237−1247.

(32) Han, S. S.; Mendoza-Cortes, J. L.; Goddard, W. A. *Chem. Soc. Rev.* **2009**, *38*, 1460−1476.
(33) Sillar, K.; Hofmann, A.; Sauer, J. *J. Am. Chem. Soc.* **2009**, *13*, 4143−4150.
(34) Fowler, R. H.; Guggenheim, E. A. *Statistical thermodynamics: a version of statistical mechanics for students of physics and chemistry*; University Press: Cambridge, U.K., 1956.
(35) Young, D. M.; Crowell, A. D. *Physical adsorption of gases*; Butterworths: London, 1962.
(36) Zhou, W.; Wu, H.; Yildirim, T. *J. Am. Chem. Soc.* **2008**, *130*, 15268−15269.
(37) Grimme, S. *J. Comput. Chem.* **2006**, *27* (15), 1787−1799.
(38) Kong, L.; Roman-Perez, G.; Soler, J. M.; Langreth, D. C. *Phys. Rev. Lett.* **2009**, *103*, 096103.
(39) Nijem, N.; Veyan, J.-F.; Kong, L.; Wu, H.; Zhao, Y.; Li, J.; Langreth, D. C.; Chabal, Y. J. *J. Am. Chem. Soc.* **2010**, *132*, 14834−14848.
(40) Tuma, C.; Sauer, J. *Phys. Chem. Chem. Phys.* **2006**, *8*, 3955−3965.
(41) Svelle, S.; Tuma, C.; Rozanska, X.; Kerber, T.; Sauer, J. *J. Am. Chem. Soc.* **2008**, *130*, 816−825.
(42) Tuma, C.; Kerber, T.; Sauer, J. *Angew. Chem., Int. Ed.* **2010**, *49*, 4678−4680.
(43) Valenzano, L.; Civalleri, B.; Sillar, K.; Sauer, J. *J. Phys. Chem. C* **2011**, *115* (44), 21777−21784.
(44) Kresse, G.; Furthmüller, J. *Comput. Mater. Sci.* **1996**, *6*, 15−50.
(45) Kresse, G.; Furthmuller, J. *Phys. Rev. B* **1996**, *54*, 11169−11186.
(46) Kerber, T.; Sierka, M.; Sauer, J. *J. Comput. Chem.* **2008**, *29*, 2088−2097.
(47) Monkhorst, H. J.; Pack, J. D. *Phys. Rev. B* **1976**, *13*, 5188−5192.
(48) Hättig, C.; Weigend, F. *J. Chem. Phys.* **2000**, *113*, 5154−5161.
(49) Hättig, C.; Hellweg, A.; Köhn, A. *Phys. Chem. Chem. Phys.* **2006**, *8*, 1159−1169.
(50) Ahlrichs, R.; Bär, M.; Häser, M.; Horn, H.; Kölmel, C. *Chem. Phys. Lett.* **1989**, *162*, 165−169.
(51) Ahlrichs, R.et al.*TURBOMOLE*, V6.3; TURBOMOLE GmbH: Karlsruhe, Germany, 2011.
(52) Dunlap, B. I.; Conolly, J. W. D.; Sabin, J. R. *J. Chem. Phys.* **1979**, *71*, 4993−4999.
(53) Dunning, T. H., Jr. *J. Chem. Phys.* **1989**, *90*, 1007−1023.
(54) Kendall, R. A.; Dunning, T. H., Jr.; Harrison, R. J. *J. Chem. Phys.* **1992**, *96*, 6796−6806.
(55) Weigend, F; Häser, M.; Patzelt, H.; Ahlrichs, R. *Chem. Phys. Lett.* **1998**, *294*, 143.
(56) Hellweg, A.; Hättig, C.; Höfener, S.; Klopper, W. *Theor. Chem. Acc.* **2007**, *117*, 587−597.
(57) Weigend, F.; Köhn, A.; Hättig, C. *J. Chem. Phys.* **2002**, *116*, 3175−3183.
(58) Boys, S. F.; Bernardi, F. B. *Mol. Phys.* **1970**, *19*, 553−566.
(59) Halkier, A.; Helgaker, T.; Jørgensen, P.; Klopper, W.; Olsen, J. *Chem. Phys. Lett.* **1999**, *302*, 437−446.
(60) Jensen, F. *Theor. Chem. Acc.* **2005**, *113*, 267−273.
(61) Helgaker, T.; Klopper, W.; Koch, H.; Noga, J. *J. Chem. Phys.* **1997**, *106*, 9639−1997.
(62) Valenzano, L.; Civalleri, B.; Chavan, S.; Palomino, G. T.; Arean, C. O.; Bordiga, S. *J. Phys. Chem. C* **2010**, *114*, 11185−11191.
(63) Sherrill, C. D.; Takatani, T.; Hohenstein, E. G. *J. Phys. Chem. A* **2009**, *113*, 10146−10159.
(64) Li, A. H.-T.; Chao, S. D. *J. Mol. Struct.: THEOCHEM* **2009**, *897*, 90−94.
(65) Matanović, I.; Xu, M.; Moskowitz, J. W.; Eckert, J.; Bačić, Z. *J. Chem. Phys.* **2009**, *131*, 224308−224315.
(66) Khaliullin, R. Z.; Bell, A. T.; Kazansky, V. B. *J. Phys. Chem. A* **2001**, *105*, 10454−10461.
(67) Kazanskii, V. B.; Serykh, A. I.; Bell, A. T. *Kinet. Catal.* **2002**, *43*, 419−426.
(68) Larese, J. Z.; Arnold, T.; Barbour, A.; Frazier, L. R. *Langmuir* **2009**, *25*, 4078−4083.
(69) Larese, J. Z.; Marero, D. M. y.; Sivia, D. S.; Carlile, C. J. *Phys. Rev. Lett.* **2001**, *87*, 206102−206104.
(70) Moor, B. A. D.; Reyniers, M.-F.; Marin, G. B. *Phys. Chem. Chem. Phys.* **2009**, *11*, 2939−2958.
(71) Cramer, C. J. *Essentials of Computational Chemistry - Theory and Models*; Wiley: Chichester, U.K., 2002.
(72) Ambrose, D.; Tsonopoulos, C. *J. Chem. Eng. Data* **1996**, *40*, 531−546.
(73) Salem, M. M. K.; Braeuer, P.; Szombathely, M. v.; Heuchel, M.; Harting, P.; Quitzsch, K. *Langmuir* **1998**, *14*, 3376−3389.
(74) Murata, K.; El-Merraoui, M.; Kaneko, K. *J. Chem. Phys.* **2001**, *114*, 4196−4205.
(75) Myers, A. L.; Monson, P. A. *Langmuir* **2002**, *18*, 10261−10273.
(76) Mertens, F. O. *Surf. Sci.* **2009**, *603*, 1979−1984.
(77) Zhou, W.; Wu, H.; Hartman, M. R.; Yildirim, T. *J. Phys. Chem. C* **2007**, *111*, 16131−16137.
(78) Jones, A. H. *J. Chem. Eng. Data* **1960**, *5*, 196−200.
(79) Majer, V.; Svoboda, V. *Enthalpies of Vaporization of Organic Compounds: A Critical Review and Data Compilation*; IUPAC Chemical Data Series No. 32; Blackwell Scientific Publications: Oxford, U.K., 1985.